

Outflowing Gas in the Planetary Nebula K 3-54

XIUHUI CHEN,¹ DEJIAN LIU,² PING YAN,³ BINGGANG JU,³ DENGRONG LU,³ AND YINGJIE LI³

¹*College of Mathematics and Physics, Hunan University of Arts and Science, Changde 415000, China*

²*College of Science, China Three Gorges University, Yichang 443002, China*

³*Purple Mountain Observatory, Chinese Academy of Sciences, Nanjing 210008, China*

ABSTRACT

As planetary nebulae (PNe) evolve, they develop slow and strong dust-driven stellar winds, making the joint study of dust and gas essential for understanding their nature. As a pilot investigation, we selected PN K 3-54 as our target, the only known PN in the Milky Way to exhibit infrared emission from both graphene (C₂₄) and fullerene (C₆₀). The gas is traced via molecular line emissions from ¹²CO, ¹³CO, and C¹⁸O ($J = 1 \rightarrow 0$), observed using the 13.7 m telescope of the Purple Mountain Observatory. We investigate the dynamics of this PN and identify a bipolar outflow. Preliminary results suggest that the large dynamical timescale of the outflow and the weak shock environment may account for the simultaneous survival of C₂₄ and C₆₀ within and around PN K 3-54.

Keywords: Planetary nebulae (1249); circumstellar matter (241); Interstellar dynamics (839); Jets (870); Stellar winds (1636); Stellar mass loss (1613); Interstellar molecules (849); Astrochemistry (75)

1. INTRODUCTION

Most low- to intermediate-mass stars (i.e., those with masses of 1–8 M_{\odot}) evolve from the main sequence through the asymptotic giant branch (AGB) phase, during which they produce dust-rich stellar winds (Castro-Carrizo et al. 2010; Höfner & Olofsson 2018). Following the AGB phase, stars transition to the protoplanetary nebula (PPN) stage and eventually evolve into planetary nebula (PN). These stages lead to the formation of a wide variety of nonspherical structures, including elliptical, bipolar, and multipolar geometries (e.g., Balick & Frank 2002; Sahai et al. 2007). During the transition from the AGB to PPN stage, stars also exhibit high-velocity outflows, with typical expansion velocities exceeding 50–100 km s⁻¹ (Bujarrabal et al. 2001; Sánchez Contreras & Sahai 2012).

A PN represents an evolutionary stage in which slow, intense, dust-driven winds (a hallmark of the later stages of AGB evolution) become ionized (García-Hernández et al. 2012). Immediately following the AGB phase, dust undergoes numerous physical and chemical processes within PNe, including the formation of fullerene C₆₀ (Zhang & Kwok 2011); the most widely accepted mechanisms for fullerene formation include the photochemical processing of large polycyclic aromatic hydrocarbons (Berné & Tielens 2012) or the photochemical processing or destruction of hydrogenated amorphous carbon grains (García-Hernández et al. 2010; Gómez-Muñoz et al. 2024). As a relatively stable molecule, fullerene may remain intact (almost) indefinitely in space, potentially playing an important role in circumstellar and/or interstellar chemistry and physics. Indeed, García-Hernández et al. (2012) detected infrared (IR) fullerene (C₆₀) emission from 16 out of 263 PNe (a detection rate of $\sim 6\%$), as well as IR graphene (C₂₄) emission in three PNe. PN K 3-54 is the only PN in the Milky Way (MW) to exhibit both C₆₀ and C₂₄ emissions, a peculiarity that motivated our investigation into the dynamics of this object.

Given that PNe develop slow and strong dust-driven winds, and that dust coexists with gas, we, for the first time, use molecular gas to explore the dynamics of PN K 3-54. This approach aims to investigate the dynamical environments required for the survival of fullerene (C₆₀) and graphene (C₂₄) within a PN. CO spectral lines are the most commonly used tracers to reveal outflow activity in star-forming regions (e.g., Shu et al. 1987; Li et al. 2018), and have been employed to estimate the mass

and momentum of outflowing gas entrained in the stellar winds of protostars (e.g., [Bachiller 1996](#)). CO line emission has also become an important tool for studying dynamics of stellar-mass objects at various evolutionary stages, including the AGB and PN phases (e.g. [Bujarrabal et al. 2001](#); [Castro-Carrizo et al. 2010](#); [Alonso-Hernández et al. 2024](#)). For instance, [Alonso-Hernández et al. \(2024\)](#) used CO line emission to calculate the mass loss from a sample of AGB stars; [Bujarrabal et al. \(2001\)](#) determined the mass, momentum, and kinetic energy of the bipolar winds in a sample of PPNe; and [Lorenzo et al. \(2021\)](#) estimated the mass loss in a sample of PPNe and young PNe.

In this pilot study, we focus on the unique PN K 3-54, which exhibits IR emission from both C_{60} and C_{24} , to investigate its dynamics using CO line emission. The remainder of the paper is organized as follows. Section 2 describes the observations used in this work. Section 3 presents the results, including the identification of a bipolar outflow in PN K 3-54. Section 4 discusses the distance and physical properties of PN K 3-54. Finally, Section 5 gives a summary.

2. OBSERVATIONS

From 2022 May to December, we observed PN K 3-54 using the 13.7 m telescope of the Purple Mountain Observatory (PMO 13.7 m telescope, hereafter). Three molecular lines were simultaneously observed: ^{12}CO ($J = 1 \rightarrow 0$) (115.271 GHz) with a half-power beam width (HPBW) of $\sim 50''$, ^{13}CO ($J = 1 \rightarrow 0$) (110.201 GHz), and C^{18}O ($J = 1 \rightarrow 0$) (109.782 GHz) with an HPBW of $\sim 52''$. These molecular lines were observed using the nine-beam Superconducting Spectroscopic Array Receiver system (SSAR) in the sideband separation mode ([Shan et al. 2012](#)), with ^{12}CO in the upper sideband and ^{13}CO and C^{18}O in the lower sideband. The system temperatures were 250–300 K for ^{12}CO and 150–200 K for ^{13}CO and C^{18}O . Observations were conducted in the on-the-fly (OTF) mode, and the OTF raw data were gridded into a FITS cube with a pixel size of $30''$ (each pixel contains a spectrum) using the GILDAS software package ([Pety 2005](#)). Each fast Fourier transform spectrometer, with a bandwidth of 1 GHz, provided 16,384 channels, resulting in a spectral resolution of 61 kHz. The corresponding velocity resolution was $\sim 0.16 \text{ km s}^{-1}$ for ^{12}CO and $\sim 0.17 \text{ km s}^{-1}$ for ^{13}CO and C^{18}O . All results presented in this work are expressed as brightness temperatures, T_b . The total size of the map is $\sim 20'$ with a total integration time of $\sim 3 \text{ hr}$.

3. RESULTS

This section describes the channel map and the identification of a bipolar outflow in PN K 3-54.

3.1. *Channel Map of PN K 3-54*

Two components are clearly visible in the channel map shown in Figure 1. The velocity watershed of these two components is at $\sim 8.5\text{--}9.0\text{ km s}^{-1}$. This velocity watershed corresponds to the systemic velocity, which is more precisely determined to be $\sim 8.6\text{ km s}^{-1}$, as shown in Figure 2(c)-(d). The blue (low-velocity) component (see the dotted blue ellipse) begins to appear at a velocity of $\sim 6.5\text{ km s}^{-1}$, reaching its peak emission at $\sim 7.5\text{--}8.0\text{ km s}^{-1}$, and fades out at $\sim 8.5\text{ km s}^{-1}$. For the red (high-velocity) component (see the dotted red ellipse), the corresponding velocities are ~ 9.0 , $\sim 9.5\text{--}10$, and $\sim 11.0\text{ km s}^{-1}$, respectively. The figure exhibits a pronounced bipolar structure with a southeast-northwest orientation, which we identify as a bipolar outflow in PN K 3-54 (see below).

In addition, another bipolar elongated structure with a very small velocity span is visible in Figure 1. This structure consists of a low-velocity component at $\sim 8.0\text{--}8.5\text{ km s}^{-1}$ (see the dashed blue ellipse in Figure 1) and a high-velocity component at $\sim 9.0\text{--}9.5\text{ km s}^{-1}$ (see the dashed red ellipse). The blue elongated structure is located to the southeast of PN K 3-54 (denoted by a lime star) and is aligned along a southeast–northwest direction, while the red elongated structure, located to the west of the blue structure, exhibits an east–west orientation. This possible bipolar structure may trace a slow outflow roughly along the east-west direction. If confirmed by three-dimensional maps with high spatial and velocity resolution, the presence of two bipolar outflows with different orientations may suggest that the orientation of the stellar winds driven by the central star varies over time.

3.2. *Outflow Identification*

An outflow can be inferred and characterized based on three aspects: the spectral line profiles, the spatial distribution of the blue and red lobes (traced by the integrated intensity map of each lobe), and the position–velocity (P-V) diagram. PNe exhibit a bimodal line profile in CO emission, as shown by Castro-Carrizo et al. (2010) and Lorenzo et al. (2021). This bimodal line profile suggests that a large number of ejections have accumulated around PNe, with the broad line wings serving

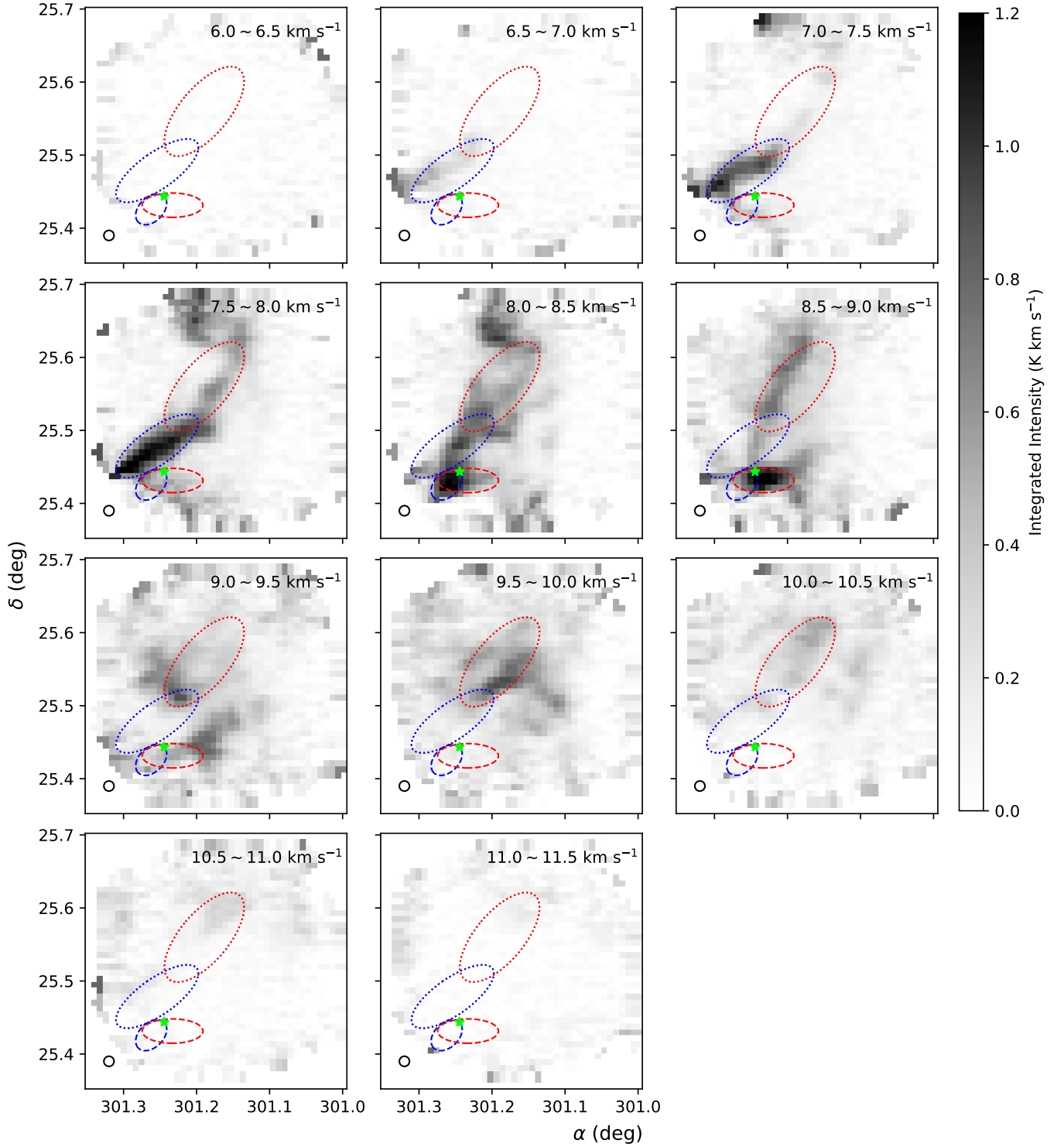


Figure 1. PN K 3-54 ^{13}CO channel map, where α and δ are the R.A. and Decl. (J2000), respectively. The black open circle represents the beam size of ^{13}CO , and the lime star denotes PN K 3-54. The dotted ellipses outline a pronounced bipolar structure (see Figure 2), and the dashed ellipses indicate a possible bipolar outflow that requires further confirmation.

as tracers of these ejections. Therefore, throughout this work, regions corresponding to the bimodal line profile are treated as outflowing gas components.

Figure 2 shows a clear bipolar outflow traced by ^{13}CO emission in PN K 3-54. Panel (a) presents an integrated intensity map of C^{18}O with the ^{13}CO blue and red lobe contours overplotted. The integrated intensity map of C^{18}O shows the overall distribution of gas across the region. The red and blue lobes of ^{13}CO (see the red and blue dotted ellipses, respectively) demonstrate relatively symmetric, clearly elongated structures with high collimation (i.e., the major/minor axis radii of the red and blue ellipses are $\sim 2.3'$ and $2.7'$, respectively). Panel (b) shows a P-V diagram along the direction connecting the peak emission from the red and blue lobes (see the white arrows in panel (a)). Panels (c) and (d) show velocity profiles and selected velocity intervals of the line wings (see the shaded regions), where spectra of the blue and red lobes are extracted from pixels corresponding to the peak integrated intensity of the respective lobes. Given that the line wings are relatively faint, we selected the brightest pixels to more effectively capture the spectral line profiles of the line wings. The inspection of the entire figure reveals a clear bipolar outflow structure in PN K 3-54, evident in the spectral line profiles, spatial distributions of the blue and red lobes, and the P-V diagram. The bimodal line profiles shown in panels (c) and (d) are characteristic of PNe (e.g., [Castro-Carrizo et al. 2010](#); [Lorenzo et al. 2021](#)), suggesting that the excitation source for this bipolar outflow is probably the central source of PN K 3-54.

4. DISCUSSION

4.1. *Estimation of Distance*

The distance to PN K 3-54 was assumed to be 23.4 kpc by [Stanghellini & Haywood \(2010\)](#) and [García-Hernández et al. \(2012\)](#). The parallax from Gaia Data Release 3 (DR3) of the corresponding star is -0.04 ± 0.13 mas (the Gaia DR3 ID: 1834720521736114816; [Gaia Collaboration et al. 2021](#)), indicating that no effective distance is provided. For stars with a poorly determined or unknown Gaia parallax, [Bailer-Jones et al. \(2021\)](#) attempted to determine stellar distances by combining the colors and apparent magnitudes of stars with known parallaxes. This approach assumes that a star

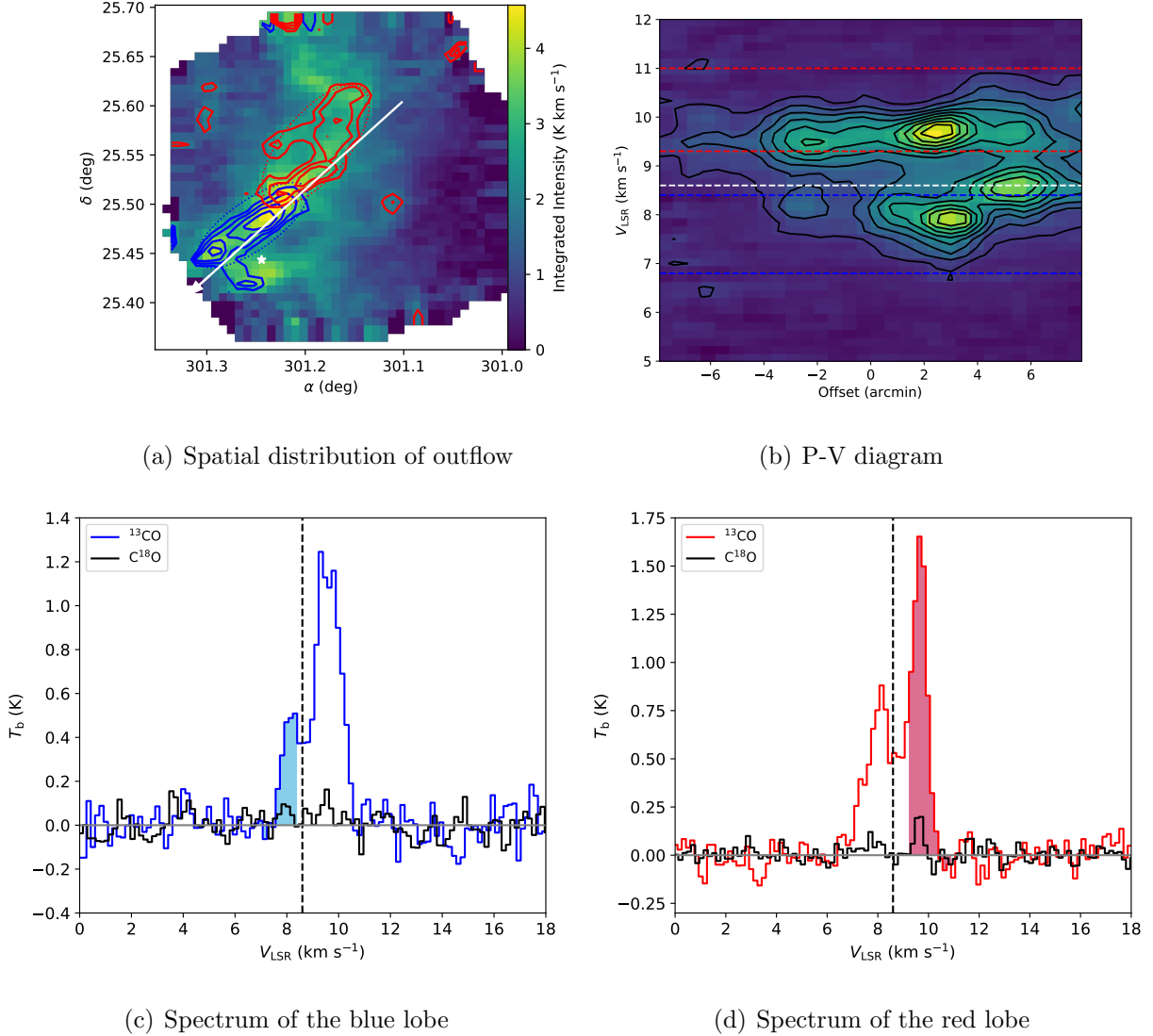


Figure 2. Outflowing gas in PN K 3-54 identified by ^{13}CO emission. (a) Integrated C^{18}O map with ^{13}CO blue and red lobe contours overlotted. The contour levels range from 60% to 90% with steps of 10% of the peak intensity of each lobe. The lengths of the major axes of the ellipses, representing the red and blue lobes, are used to estimate the length of outflow lobes. The white star represents PN K 3-54, and α and δ refer to R.A. and Decl. (J2000), respectively. (b) P-V diagram along the white arrow in panel (a). The black contour levels range from 10% to 90% with steps of 10% of the peak value. The blue and red dashed lines show the velocity intervals of the blue and red lobes, respectively. The white dashed line indicates the systemic velocity of PN K 3-54. (c) Spectra of ^{13}CO and C^{18}O , shown in blue and black, respectively, at the pixel corresponding to the peak position of the blue emission of the ^{13}CO outflow. The blue shading in the spectrum indicates the blue line wing velocity of ^{13}CO , and the black dash line shows the systemic velocity. (d) The spectra of ^{13}CO and C^{18}O , shown in red and black, respectively, at the pixel corresponding to the peak position of the red emission of the ^{13}CO outflow. The red shading in the spectrum indicates the red line wing velocity of ^{13}CO , and the black dash line shows the systemic velocity.

with a given color has a limited number of possible absolute magnitudes (plus extinction). For the star of interest in this work, [Bailer-Jones et al. \(2021\)](#) derived a median distance of $4.087^{+0.906}_{-1.718}$ kpc. However, the actual degree of extinction toward PN K 3-54 affects the reliability of the distance inferred by this method. [Nataf et al. \(2016\)](#) argued that the extinction law varies across the inner Galaxy, and the Galactic coordinates of PN K 3-54 are $l \sim 63.8^\circ$ and $b \sim -3.3^\circ$, respectively.

The kinematic distance to PN K 3-54 was determined using the model developed by [Reid et al. \(2016, 2019\)](#), which applies a Bayesian approach to distance estimation. This method integrates the MW's rotation curve, Galactic coordinates, radial velocity, and other available data, such as proper motion. ¹The key parameters for estimating the kinematic distance are the Galactic coordinates, and the radial velocity, V_{LSR} , of the target source. Figure 3 presents the spectra of PN K 3-54. The red line wing (corresponding to the red lobe of the bipolar outflow in Figure 2) is centered at $\sim 9.5 \text{ km s}^{-1}$, as indicated in both the spectrum from ^{12}CO (Figure 3) and the ^{13}CO spectra at the peak emission of the blue and red lobes (see panels (c) and (d) of Figure 2) of PN K 3-54. The blue line wing (corresponding to the blue lobe of the bipolar outflow in Figure 2) is blended with a core component in the ^{12}CO spectrum and obscured by noise in the ^{13}CO spectrum (Figure 3). Fortunately, the blue line wing is visible at other positions (e.g., panels (c) and (d) in Figure 2) with a central velocity of $\sim 7.6 \text{ km s}^{-1}$. The central velocity of the core component (i.e, the systemic velocity) is pronounced at $\sim 8.6 \text{ km s}^{-1}$ when combining the ^{13}CO spectra in panels (c) and (d) of Figure 2 with the ^{12}CO spectrum in Figure 3. Adopting the values of l , b and V_{LSR} as 63.80° , -3.30° , and 8.6 km s^{-1} , respectively, the corresponding kinematic distance estimate,² following [Reid et al. \(2019\)](#), is roughly $\sim 0.4 \pm 0.8$ kpc. This distance of 0.4 kpc is adopted as the final distance to PN K 3-54 (see below).

4.2. Physical Properties

The physical properties of the bipolar outflow in PN K 3-54, traced by ^{13}CO line emission, were calculated assuming a distance of 0.4 kpc. Under the assumption of local thermodynamic equilibrium

¹ This approach constructs a probability density function (PDF) for each type of available distance information, and these PDFs are subsequently multiplied to obtain a combined distance PDF. The final distance is determined from the combined distance PDF.

² See <http://bessel.vlbi-astrometry.org/node/378>

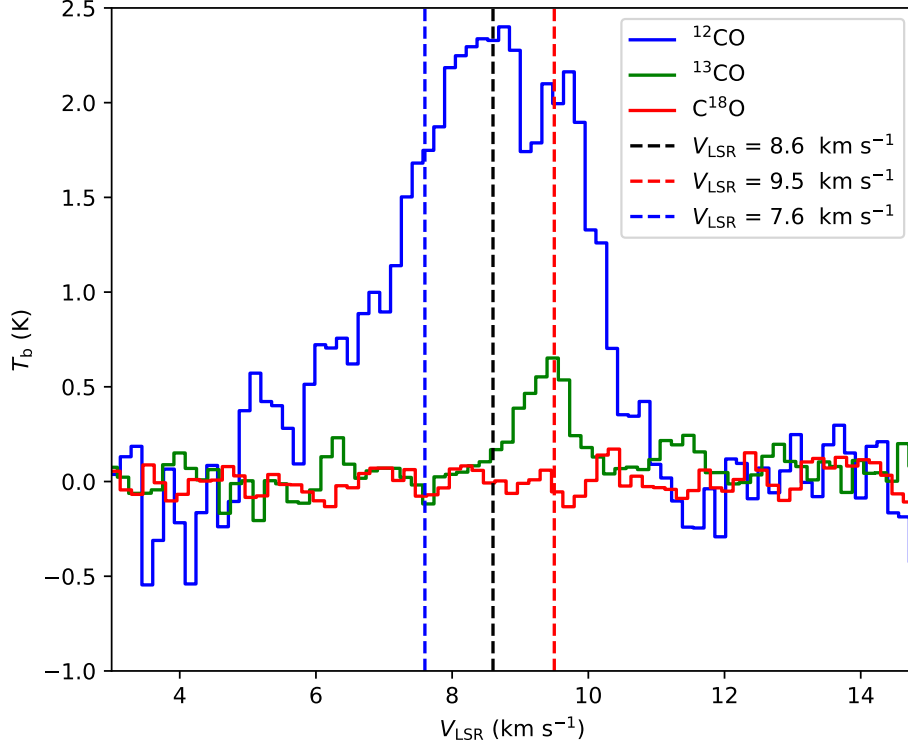


Figure 3. Spectra centered on PN K 3-54, where the blue, green and red lines represent the spectra of ^{12}CO , ^{13}CO , and C^{18}O , respectively. The rms values for these three spectra are 0.21, 0.09, and 0.08 K, respectively. The black, red, and blue vertical lines indicate the systemic velocity and the velocities at the peak emission of the red and blue lobes, respectively. The threshold for a confirmed detection is that the values of T_b in three consecutive channels (corresponding to $\sim 0.5 \text{ km s}^{-1}$) exceed $3 \times \text{rms}$. Although no C^{18}O emission was detected, the C^{18}O spectrum is included here for reference, providing further context for this region.

(LTE), the H_2 column density, N_{lobe} , of the outflow lobe is derived from (Wilson et al. 2013)

$$N_{\text{lobe}} = \frac{4.6 \times 10^{13}}{X(^{13}\text{CO})} \frac{T_{\text{ex}}}{e^{-5.3/T_{\text{ex}}}} \int T_b dv, \quad (1)$$

where the velocity range corresponds to the line wing interval (see Figure 2). The abundance of ^{13}CO is assumed to be $X(^{13}\text{CO}) = [^{13}\text{CO}]/[\text{H}_2] = 2 \times 10^{-5}$ (Bujarrabal et al. 2001). The excitation temperature, T_{ex} , is taken as the dust temperature determined by Planck (Planck Collaboration et al. 2011, 2016) in this region, which is 18 K, similar to the value used by Bujarrabal et al. (2001). The relative uncertainty in N_{lobe} due to T_{ex} is less than 50%, assuming T_{ex} ranges from 10 to 30 K. Because

there is only one component of ^{12}CO emission (with a systemic velocity of $\sim 8.6 \text{ km s}^{-1}$) within the velocity range of $[-100, 100] \text{ km s}^{-1}$, dust is probably associated with this component. The mass of the outflow lobe is

$$M_{\text{lobe}} = N_{\text{lobe}} A_{\text{lobe}} \mu m_{\text{H}}, \quad (2)$$

where A_{lobe} is the area enclosing 60% of the peak of outflow lobe, $\mu = 2.72$ is the average molecular mass, and m_{H} is the mass of the hydrogen atom (Garden et al. 1991).

We also calculated the momentum, P_{lobe} , and kinetic energy, E_{lobe} , of the outflow lobe, as well as the average velocity (i.e., the relative velocity with respect to the systemic system, weighted by T_{b}), $\langle \Delta v_{\text{lobe}} \rangle$,

$$P_{\text{lobe}} = \sum_{A_{\text{lobe}}} M_{\text{lobe}} \langle \Delta v_{\text{lobe}} \rangle, \quad (3)$$

$$E_{\text{lobe}} = \sum_{A_{\text{lobe}}} M_{\text{lobe}} \langle \Delta v_{\text{lobe}}^2 \rangle, \quad (4)$$

where $\langle \Delta v_{\text{lobe}}^2 \rangle$ represents the square of the average velocity (for further details, see Li et al. 2018; Liu et al. 2021). Additionally, we calculated the dynamical timescale, t_{lobe} , the mechanical luminosity, L_{lobe} , and the mass-loss rate, \dot{M}_{lobe} , of the outflow lobe:

$$t_{\text{lobe}} = l_{\text{lobe}} / \Delta v_{\text{max}}, \quad (5)$$

$$L_{\text{lobe}} = E_{\text{lobe}} / t_{\text{lobe}}, \quad (6)$$

$$\dot{M}_{\text{lobe}} = M_{\text{lobe}} / t_{\text{lobe}}, \quad (7)$$

where l_{lobe} is the length of the outflow lobe, which was estimated from the ellipses shown in Figure 2(a), and Δv_{max} is the maximum velocity of the outflow lobe. The values of Δv_{max} for the red and blue lobes are equal to the absolute value of the maximum velocity difference between the velocity indicated by the white line and those of the red and blue lines, respectively, as shown in Figure 2(b).

Assuming a random distribution of inclination angles, the mean value of inclination angle is given by $\langle \theta \rangle = \int_0^{\pi/2} \theta \cos \theta d\theta \sim 33^\circ$ (i.e., the same as that adopted in Bujarrabal et al. 2001, where the inclination angle is not known). The corrections for an inclination angle of 33° to the values of $\langle \Delta v_{\text{lobe}} \rangle$, l_{lobe} , P_{lobe} , E_{lobe} , t_{lobe} , L_{lobe} , and \dot{M}_{lobe} are $1/\sin \theta = 1.8$, $1/\cos \theta = 1.2$, $1/\sin \theta = 1.8$,

$1/\sin^2\theta = 3.4$, $\sin\theta/\cos\theta = 0.6$, $\cos\theta/\sin^3\theta = 5.2$, and $\cos\theta/\sin\theta = 1.5$, respectively. On the other hand, if the true inclination of the outflow with respect to the plane of the sky is close to 0° , we may significantly underestimate $\langle\Delta v_{\text{lobe}}\rangle$, P_{lobe} , E_{lobe} , L_{lobe} , and \dot{M}_{lobe} . The probability that θ is smaller than 20° , assuming a random distribution of the outflow axes, is ~ 0.40 . Therefore, with a probability of $\sim 60\%$, the underestimates for the values of $\langle\Delta v_{\text{lobe}}\rangle$, P_{lobe} , E_{lobe} , L_{lobe} , and \dot{M}_{lobe} are smaller by factors of 1.6, 1.6, 2.5, 4.5, and 1.8, respectively. However, for the values of l_{lobe} and t_{lobe} , the corrections for inclination angles of 20° (which are 1.1 and 0.4, respectively) are smaller than those for inclination angles of 33° .

Table 1 lists the physical properties of the outflow lobe, corrected for the inclination angle (assuming $\theta = 33^\circ$), with $\langle\Delta v_{\text{lobe}}\rangle$ as the only physical parameter independent of distance. Note that the distance is embedded in the units of the results presented in the table due to the large uncertainty in the distance. If the distance to PN K 3-54 is 23.4 kpc, the value of l_{lobe} would be ~ 7 pc, which exceeds the maximum size a PN could eventually reach (see [Dopita & Meatheringham 1991](#); [Pierce et al. 2004](#); [Parker 2022](#)), suggesting that this distance is likely an overestimate. With a distance of ~ 4 kpc, the sum of mass of the blue and red lobes would be $\sim 218 M_\odot$, which far exceeds the mass of the outflows observed toward PPNe as reported by [Bujarrabal et al. \(2001\)](#). Similarly, the sum of the mass-loss rates of the blue and red lobes would reach $1.1 \times 10^{-3} M_\odot \text{ yr}^{-1}$, a value that is also much higher than those measured for AGB and early post-AGB circumstellar envelopes ([Castro-Carrizo et al. 2010](#)), and for PPNe and young PNe ([Lorenzo et al. 2021](#)). These values suggest that the distance of ~ 4 kpc is also likely an overestimate. Therefore, the adopted distance to PN K 3-54 of ~ 0.4 kpc seems more reasonable. Note, however, the actual distance requires further confirmation.

The average dynamical timescale, t_{lobe} , for the two lobes is $\sim 1.9 \times 10^4$ yr. Even assuming $\theta = 20^\circ$, the average dynamical timescale decreases to $\sim 1.1 \times 10^4$ yr, which is larger than the dynamical ages of PNe reported in previous studies (i.e., ~ 400 – 10000 yr, [Guillén et al. 2013](#); [Danekkar 2022](#); [Gómez-Muñoz et al. 2023](#); [Derlopa et al. 2024](#)). The average value of the average velocity, $\langle\Delta v_{\text{lobe}}\rangle$ (independent of distance), of the two lobes is only $\sim 3.8 \text{ km s}^{-1}$. Even assuming $\theta = 20^\circ$, $\langle\Delta v_{\text{lobe}}\rangle$ increases to only $\sim 6 \text{ km s}^{-1}$, which is still smaller than the values traced by CO line emission for

Table 1. Physical Properties of the Outflow PN K 3-54 with Inclination Correction

Lobe	N_{lobe} (10^{20} cm^{-2})	M_{lobe} $\left(\frac{d^2}{0.16} M_{\odot}\right)$	$\langle \Delta v_{\text{lobe}} \rangle$ (km s^{-1})	l_{lobe} $\left(\frac{d}{0.4} \text{ pc}\right)$	P_{lobe} $\left(\frac{d^2}{0.16} M_{\odot} \text{ km s}^{-1}\right)$	E_{lobe} $\left(\frac{d^2}{0.16} 10^{44} \text{ erg}\right)$	t_{lobe} $\left(\frac{d}{0.4} 10^4 \text{ yr}\right)$	L_{lobe} $\left(\frac{d}{0.4} L_{\odot}\right)$	\dot{M}_{lobe} $\left(\frac{d}{0.4} M_{\odot} 10^{-5} \text{ yr}^{-1}\right)$
blue	1.3	1.3	3.1	0.1	7.4	4.1	2.1	1.0	6.0
red	0.7	0.9	4.5	0.1	7.9	6.8	1.7	1.6	5.7
Mean	2.0	1.1	3.8	0.1	7.7	5.5	1.9	1.3	3.8
Sum	...	2.2	15.3	10.9	...	2.6	11.3

Note. d denotes the actual distance to PN K 3-54.

PPNe, compact PNe, and extended PNe, as reported by [Lorenzo et al. \(2021\)](#). This suggests that PN K 3-54 may be in a relatively weak shock environment. The mass-loss rate, \dot{M}_{lobe} , of PN K 3-54 is larger than those of AGB and early post-AGB circumstellar envelopes as determined by [Castro-Carrizo et al. \(2010\)](#) and compact PNe as measured by [Lorenzo et al. \(2021\)](#), but it is comparable to the results found for PPNe and extended PNe by [Lorenzo et al. \(2021\)](#).

Other physical parameters, such as N_{lobe} , M_{lobe} , P_{lobe} , E_{lobe} , and L_{lobe} , are also listed in Table 1. The maximum column density, N_{lobe} , for the two lobes is lower than the values reported by [Alonso-Hernández et al. \(2024\)](#), who focused on the envelopes of AGB star (note that they listed column densities of CO). The total value of M_{lobe} is greater than the majority of the values reported by [Bujarrabal et al. \(2001\)](#), who focused on PPNe. Meanwhile, total values of P_{lobe} and E_{lobe} fall within the ranges of corresponding values found for fast outflows in the study by [Bujarrabal et al. \(2001\)](#).

In summary, from the perspective of gas dynamics, the outflow velocity $\langle \Delta v_{\text{lobe}} \rangle$ in PN K 3-54 is relatively smaller compared to that of outflows from AGB stars, PPNe, and PNe, indicating that PN K 3-54 may be in a weak shock environment. The dynamical timescale may exceed the kinematical ages of PNe. The survival of C₂₄ and C₆₀ in the environment within and surrounding PN K 3-54 may be attributed to the large dynamical timescale and the weak shocks present in the environment. However, the conditions under which C₂₄ and/or C₆₀ formed cannot be determined, as the CO gas studied here is likely not close enough to the central star due to the moderate spatial resolution. In future studies, we will explore the potential correlation between the gas dynamics of PNe and their carbonaceous dust IR emission by conducting a statistical study of CO emission from a large sample of PNe. Such an approach could provide insight into the dynamic environments of

carbonaceous dust and assess whether such dust can survive within these conditions. The formation of carbonaceous dust will also be investigated using high-spatial-resolution facilities, such as the Atacama Large Millimeter/submillimeter Array (ALMA).

5. SUMMARY AND CONCLUSION

Using ^{12}CO , ^{13}CO , and C^{18}O ($J = 1-0$) line emission observed with the PMO 13.7 m telescope, we investigated the dynamics of PN K 3-54, the only PN in the MW where IR emission from both fullerene C_{60} and graphene C_{24} has been detected. A bipolar outflow was identified in this region, and the kinematic distance to PN K 3-54 was estimated to be roughly ~ 0.4 kpc. The physical properties of this outflow were calculated, suggesting that the large dynamical timescale of outflow in PN K 3-54 and the small outflow velocity (indicative of a weak shock environment) may be the reasons why C_{24} and C_{60} can survive simultaneously within and around PN K 3-54. Further observational studies of molecular gas toward a large number of PNe are required to further confirm our conclusions.

We would like to thank the anonymous referee for the helpful comments and suggestions that helped to improve the paper. We would like to thank all the staff members of the PMO 13.7 m telescopes for their support in making the observations presented in this work. This work was funded by the Doctoral Research Initiation Fund project of the Hunan University of Arts and Science under grant numbers 19BSQD38.

REFERENCES

- Alonso-Hernández, J., Sánchez Contreras, C., & Sahai, R. 2024, *A&A*, 684, A77, doi: [10.1051/0004-6361/202347317](https://doi.org/10.1051/0004-6361/202347317)
- Bachiller, R. 1996, *ARA&A*, 34, 111, doi: [10.1146/annurev.astro.34.1.111](https://doi.org/10.1146/annurev.astro.34.1.111)
- Bailer-Jones, C. A. L., Rybizki, J., Fouesneau, M., Demleitner, M., & Andrae, R. 2021, *AJ*, 161, 147, doi: [10.3847/1538-3881/abd806](https://doi.org/10.3847/1538-3881/abd806)
- Balick, B., & Frank, A. 2002, *ARA&A*, 40, 439, doi: [10.1146/annurev.astro.40.060401.093849](https://doi.org/10.1146/annurev.astro.40.060401.093849)
- Berné, O., & Tielens, A. G. G. M. 2012, *Proceedings of the National Academy of Science*, 109, 401, doi: [10.1073/pnas.1114207108](https://doi.org/10.1073/pnas.1114207108)
- Bujarrabal, V., Castro-Carrizo, A., Alcolea, J., & Sánchez Contreras, C. 2001, *A&A*, 377, 868, doi: [10.1051/0004-6361:20011090](https://doi.org/10.1051/0004-6361:20011090)

- Castro-Carrizo, A., Quintana-Lacaci, G., Neri, R., et al. 2010, *A&A*, 523, A59, doi: [10.1051/0004-6361/201014755](https://doi.org/10.1051/0004-6361/201014755)
- Danehkar, A. 2022, *ApJS*, 260, 14, doi: [10.3847/1538-4365/ac5cca](https://doi.org/10.3847/1538-4365/ac5cca)
- Derlopa, S., Akras, S., Amram, P., et al. 2024, *MNRAS*, 530, 3327, doi: [10.1093/mnras/stae1013](https://doi.org/10.1093/mnras/stae1013)
- Dopita, M. A., & Meatheringham, S. J. 1991, *ApJ*, 377, 480, doi: [10.1086/170377](https://doi.org/10.1086/170377)
- Gaia Collaboration, Brown, A. G. A., Vallenari, A., et al. 2021, *A&A*, 649, A1, doi: [10.1051/0004-6361/202039657](https://doi.org/10.1051/0004-6361/202039657)
- García-Hernández, D. A., Manchado, A., García-Lario, P., et al. 2010, *ApJL*, 724, L39, doi: [10.1088/2041-8205/724/1/L39](https://doi.org/10.1088/2041-8205/724/1/L39)
- García-Hernández, D. A., Villaver, E., García-Lario, P., et al. 2012, *ApJ*, 760, 107, doi: [10.1088/0004-637X/760/2/107](https://doi.org/10.1088/0004-637X/760/2/107)
- Garden, R. P., Hayashi, M., Gatley, I., Hasegawa, T., & Kaifu, N. 1991, *ApJ*, 374, 540, doi: [10.1086/170143](https://doi.org/10.1086/170143)
- Gómez-Muñoz, M. A., García-Hernández, D. A., Barzaga, R., Manchado, A., & Huertas-Roldán, T. 2024, *A&A*, 682, L18, doi: [10.1051/0004-6361/202349087](https://doi.org/10.1051/0004-6361/202349087)
- Gómez-Muñoz, M. A., Vázquez, R., Sabin, L., et al. 2023, *A&A*, 676, A101, doi: [10.1051/0004-6361/202346455](https://doi.org/10.1051/0004-6361/202346455)
- Guillén, P. F., Vázquez, R., Miranda, L. F., et al. 2013, *MNRAS*, 432, 2676, doi: [10.1093/mnras/stt612](https://doi.org/10.1093/mnras/stt612)
- Höfner, S., & Olofsson, H. 2018, *A&A Rv*, 26, 1, doi: [10.1007/s00159-017-0106-5](https://doi.org/10.1007/s00159-017-0106-5)
- Li, Y., Li, F.-C., Xu, Y., et al. 2018, *ApJS*, 235, 15, doi: [10.3847/1538-4365/aaab67](https://doi.org/10.3847/1538-4365/aaab67)
- Liu, D.-J., Xu, Y., Li, Y.-J., et al. 2021, *ApJS*, 253, 15, doi: [10.3847/1538-4365/abcece](https://doi.org/10.3847/1538-4365/abcece)
- Lorenzo, M., Teyssier, D., Bujarrabal, V., et al. 2021, *A&A*, 649, A164, doi: [10.1051/0004-6361/202039592](https://doi.org/10.1051/0004-6361/202039592)
- Nataf, D. M., Gonzalez, O. A., Casagrande, L., et al. 2016, *MNRAS*, 456, 2692, doi: [10.1093/mnras/stv2843](https://doi.org/10.1093/mnras/stv2843)
- Parker, Q. A. 2022, *Frontiers in Astronomy and Space Sciences*, 9, 895287, doi: [10.3389/fspas.2022.895287](https://doi.org/10.3389/fspas.2022.895287)
- Pety, J. 2005, in *SF2A-2005: Semaine de l’Astrophysique Française*, ed. F. Casoli, T. Contini, J. M. Hameury, & L. Pagani, 721
- Pierce, M. J., Frew, D. J., Parker, Q. A., & Köppen, J. 2004, *PASA*, 21, 334, doi: [10.1071/AS04039](https://doi.org/10.1071/AS04039)
- Planck Collaboration, Ade, P. A. R., Aghanim, N., et al. 2011, *A&A*, 536, A1, doi: [10.1051/0004-6361/201116464](https://doi.org/10.1051/0004-6361/201116464)
- Planck Collaboration, Aghanim, N., Ashdown, M., et al. 2016, *A&A*, 596, A109, doi: [10.1051/0004-6361/201629022](https://doi.org/10.1051/0004-6361/201629022)
- Reid, M. J., Dame, T. M., Menten, K. M., & Brunthaler, A. 2016, *ApJ*, 823, 77, doi: [10.3847/0004-637X/823/2/77](https://doi.org/10.3847/0004-637X/823/2/77)

- Reid, M. J., Menten, K. M., Brunthaler, A., et al. 2019, *ApJ*, 885, 131,
doi: [10.3847/1538-4357/ab4a11](https://doi.org/10.3847/1538-4357/ab4a11)
- Sahai, R., Morris, M., Sánchez Contreras, C., & Claussen, M. 2007, *AJ*, 134, 2200,
doi: [10.1086/522944](https://doi.org/10.1086/522944)
- Sánchez Contreras, C., & Sahai, R. 2012, *ApJS*, 203, 16, doi: [10.1088/0067-0049/203/1/16](https://doi.org/10.1088/0067-0049/203/1/16)
- Shan, W., Yang, J., Shi, S., et al. 2012, *IEEE Transactions on Terahertz Science and Technology*, 2, 593,
doi: [10.1109/TTHZ.2012.2213818](https://doi.org/10.1109/TTHZ.2012.2213818)
- Shu, F. H., Adams, F. C., & Lizano, S. 1987, *ARA&A*, 25, 23,
doi: [10.1146/annurev.aa.25.090187.000323](https://doi.org/10.1146/annurev.aa.25.090187.000323)
- Stanghellini, L., & Haywood, M. 2010, *ApJ*, 714, 1096, doi: [10.1088/0004-637X/714/2/1096](https://doi.org/10.1088/0004-637X/714/2/1096)
- Wilson, T. L., Rohlfs, K., & Hüttemeister, S. 2013, *Tools of Radio Astronomy* (Berlin: Springer Berlin Heidelberg),
doi: [10.1007/978-3-642-39950-3](https://doi.org/10.1007/978-3-642-39950-3)
- Zhang, Y., & Kwok, S. 2011, *ApJ*, 730, 126,
doi: [10.1088/0004-637X/730/2/126](https://doi.org/10.1088/0004-637X/730/2/126)